

<sup>1</sup>  
<sup>2</sup> Дипломна робота  
Supervisor(CERN): Massimiliano Ferro-Luzzi

<sup>3</sup>  
Bereziuk Ivan

<sup>4</sup>  
18 червня 2015 р.

# 5 1 Introduction

6 <sup>1</sup> The completion of the particle content of the Standard Model (SM) with the discovery of the  
7 Higgs boson, and advances in cosmology highlight the necessity for a new level of understanding  
8 of physics Beyond the Standard Model (BSM) . At the same time, neither experiment nor theory  
9 provide clear hints of the nature or the scale of this new physics.

10 Over the next decades the Fermi-mass scale, and even beyond, will be comprehensively  
11 explored either directly by ATLAS and CMS at the LHC, or indirectly, assuming generic  
12 couplings, at experiments like LHCb, Belle2 and NA62 [4]. Hidden particles, which interact  
13 very weakly with the SM particles, are predicted in many theoretical models capable of explaining  
14 the shortcomings of the SM. A large part of their accessible parameter space remains  
15 unexplored.

16 In this situation SHIP is a recently proposed new general purpose fixed target facility at  
17 the SPS which is aimed at exploring the domain of hidden particles and make measurements  
18 with tau neutrinos. Hidden particles are predicted by a large number of models beyond the  
19 Standard Model. The high intensity of the SPS 400 GeV beam allows probing a wide variety  
20 of models containing light long-lived exotic particles with masses below  $10 \text{ GeV}/c^2$ , including  
21 very weakly interacting low-energy SUSY states.

## 22 1.1 Overview of the Experiment

23 At the energy accessible at the SPS, the hidden particles are predominantly produced in decays  
24 of hadrons, in particular in decays of charmed and beauty hadrons above the kaon mass, and  
25 in proton bremsstrahlung.

26 The detector for the direct detection of the hidden particles is designed to fully reconstruct  
27 their exclusive decays. Table 1 summarizes the main decay modes of the hidden particles in the  
28 various models considered.

Табл. 1: Summary of the main decay modes of hidden particles in various models ( $\ell = e, \mu$ ).

Models	Final states
Neutrino portal, SUSY neutralino	$\ell^\pm\pi^\mp, \ell^\pm K^\mp, \ell^\pm\rho^\mp, \rho^\pm \rightarrow \pi^\pm\pi^0$
Vector, scalar, axion portals, SUSY sgoldstino	$\ell^+\ell^-$
Vector, scalar, axion portals, SUSY sgoldstino	$\pi^+\pi^-, K^+K^-$
Neutrino portal ,SUSY neutralino, axino	$\ell^+\ell^-\nu$
Axion portal, SUSY sgoldstino	$\gamma\gamma$
SUSY sgoldstino	$\pi^0\pi^0$

29 The principal background to the hidden particle decay signal originates from the inelastic  
30 scattering of neutrinos and muons in the vicinity of the detector producing long-lived particles.

<sup>1</sup>This section mostly(The information of for this section was) taken from SHiP Technical Proposal (TP) document [3] just to overview the experiment and prepare reader for subsequent work under separate part of detector.

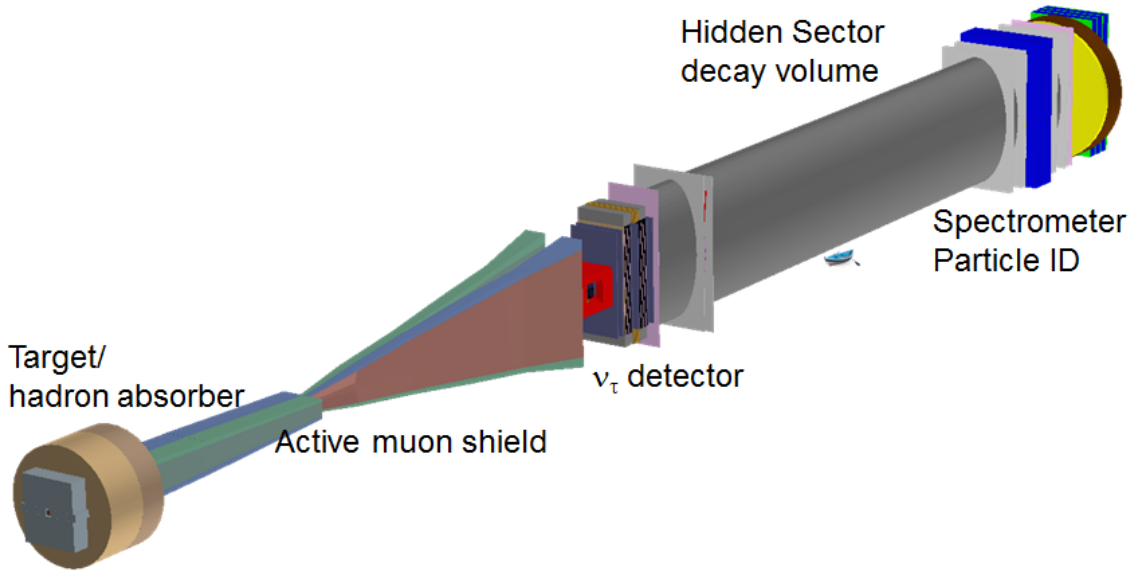


Рис. 1: Overview of the SHiP facility [3]

31     The beam line is designed to minimize the background sources. The proton interaction in  
 32     the target gives rise to a copious direct production of short-lived resonances, and pions and  
 33     kaons. While a hadron stopper of a few metres of iron is sufficient to absorb the hadrons and  
 34     the electromagnetic radiation emerging from the target, the decays of pions, kaons and short-  
 35     lived resonances result in a large flux of muons and neutrinos. In order to reduce the flux of  
 36     neutrinos, in particular the flux of muon neutrinos and the associated muons, the pions and  
 37     kaons should be stopped as efficiently as possible before they decay. The target must therefore  
 38     be made of a material with the shortest possible interaction length and be sufficiently long to  
 39     contain the hadronic showers with minimum leakage. Since the production angle of the hidden  
 40     particles is relatively large, there is no requirement to minimize the beam spot.

41     The short-lived resonances and the residual flux of decaying pions and kaons still give rise  
 42     to a large flux of muons. This flux must be efficiently cleared from the detector fiducial volume  
 43     by either a passive shield or through an active shield based on magnetic deflection. The residual  
 44     flux should also be low enough so not to compromise the occupancy limit in the tau neutrino  
 45     detector. As illustrated in Figure 1, in the baseline design a 5 m horizontally wide region  
 46     respecting these requirements has been achieved with a 48 m long active muon shield based on  
 47     magnetic deflection of the muons in the horizontal plane.

48     The muon shield is followed by the 10 m long tau neutrino detector, which puts the start  
 49     of the HS decay volume at about 64 m [3]. The main purpose of the tau neutrino detector is to  
 50     perform the first direct observation of the  $\bar{\nu}_\tau$ , and to study the properties and the cross section  
 51     of  $\nu^\tau$  and  $\bar{\nu}_\tau$ . The current optimization of muon shield and cost, results in a decay volume with  
 52     an elliptical shape of 5 m width and 10 m height. The length of the decay volume is obtained  
 53     by maximizing the acceptance to the hidden particle decay products given the transversal size.

54     The full reconstruction of the hidden particle decays requires a magnetic spectrometer and  
 55     a system for particle identification at the end of the decay volume.

56     The particle identification system requires an electromagnetic calorimeter for  $e/\gamma$  identifi-

57 fication with sufficient granularity and energy resolution in order to reconstruct  $\pi^0$ 's, and a  
 58 hadron calorimeter in combination with a muon detector for  $\pi/\mu$  separation.

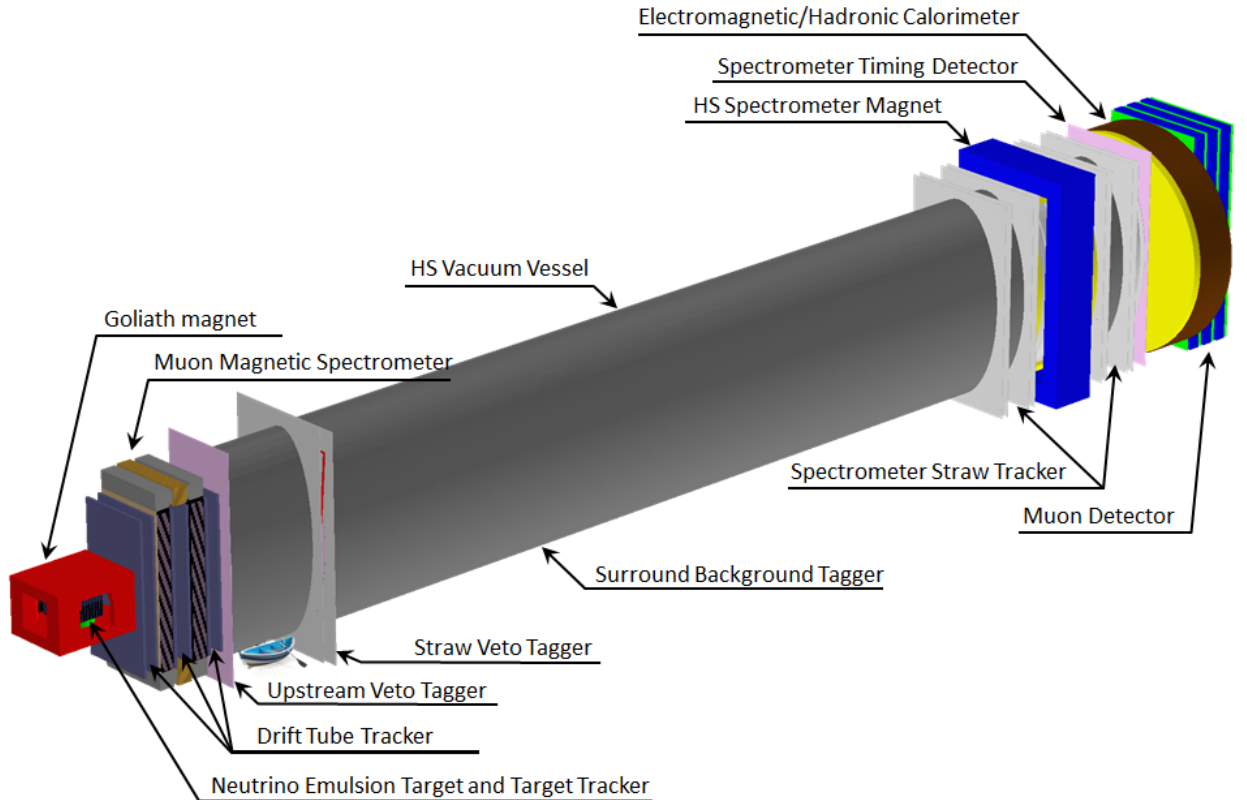


Рис. 2: SHiP detector layout

## 59 1.2 Spectrometer tracker

60 Spectrometer tracker is a part of particle identification system. The purpose of the HS  
 61 spectrometer is to reconstruct with high efficiency the tracks of charged particles from the  
 62 decay of hidden particles. The spectrometer must provide an accurate determination of the  
 63 track momentum and of the flight direction within the fiducial decay volume.

64 The spectrometer consists of a large aperture dipole magnet and two tracking telescopes on  
 65 each side of the magnet. A layout with four tracking stations symmetrically arranged around  
 66 the dipole magnet, as depicted in Figure 3a, is taken as a baseline. The size and layout of the  
 67 tracker stations is connected to the size of the magnet. A dipole spectrometer magnet with a  
 68 horizontal gap of 5 m, a height of 10 m and a length of 5 m provides good acceptance coverage  
 69 and is considered feasible at a reasonable cost.

70 Following the direction of the magnetic field, the measuring elements are oriented hori-  
 71 zontally to measure precisely the vertical (Y) coordinate. Two stereo views (U and V) are rotated  
 72 by an angle  $\pm\theta_{\text{stereo}}$  for measuring the transverse coordinate X with an accuracy degraded by  
 73  $\sim 1/\sin\theta_{\text{stereo}}$ . The precision in X (i.e. the value of the stereo angle) is driven by the need  
 74 of a good enough measurement of the decay vertex, opening angle of the daughter particles

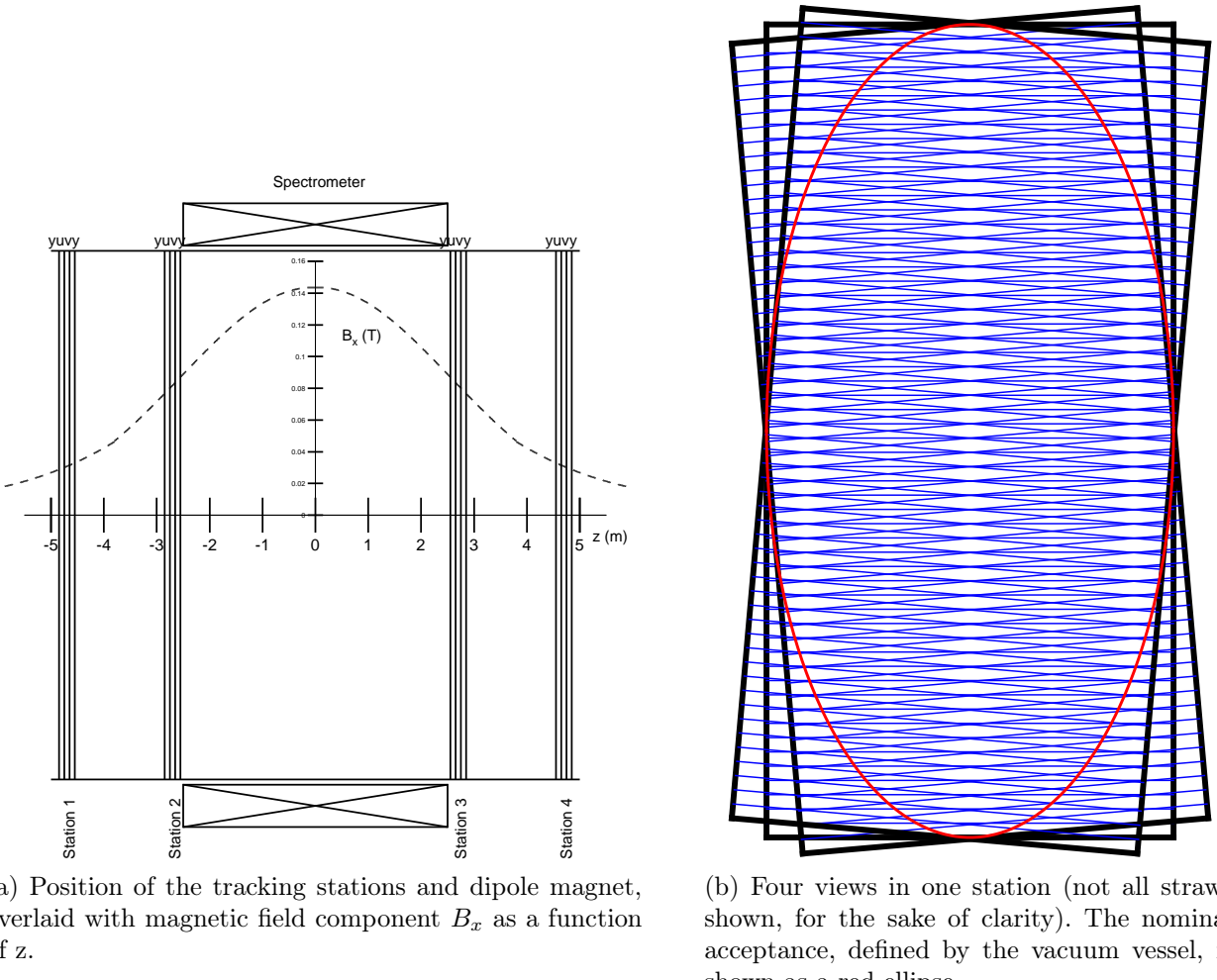


Рис. 3: Spectrometer layout

(which enters the invariant mass) and impact parameter at the production target. Each station contains 4 views (Y-U-V-Y). The two stations on the same side of the magnet are separated by  $\Delta = 2m$  and a gap of  $5m$  is left between the second and third stations (i.e. each is  $2.5m$  away from the centre of the magnet).

The tracking stations of the magnetic spectrometer must provide good spatial resolution and minimise the contribution from multiple scattering. In addition, the tracker must operate in vacuum. A straw tracker made of thin polyethylene terephthalate (PET) tubes is ideal to meet these goals. Gas tightness of these tubes has been demonstrated in long term tests and the mass production procedure is also well established (see NA62 experiment [4]). The main differences between the SHiP tracker and the NA62 tracker are the need for  $5m$  long straws (vs  $2.1\text{ m}$  in NA62). The main changes with respect to the Expression of Interest [6] follow from the changes applied to the spectrometer magnet. The straw orientation has been turned from vertical to horizontal and one transverse dimension has been increased from  $5$  to  $10\text{ m}$ .

## 88 2 Subject of study

89 With new requirements for new straw tracker we have important challenge for long straws. It  
90 is related to the fact of straw and wire will be subjected by gravitational and electrical forces  
91 and cause sagging. Because the straws are oriented horizontally (or almost, in case of stereo  
92 views), sagging is expected to cause in most drift tubes a downward deflection, which might be  
93 exploited when applying a correction.

94 Undoubtedly the presence of sagging may complicate the data processing stage and  
95 somewhat worse accuracy of track reconstruction. Primary question we have to investigate  
96 "is acceptable sag-admitting design?" and "What a downgrade of precision for sag-admitting  
97 design?".

98 Results of measurements on prototypes are discussed in Section 8.

## 99 3 Signal

100 Computer program Garfield [1] is designed for detailed simulation of two- and three-dimensional  
101 drift chambers. So we will perform STRAW tube studies using this program.

102 Charged particle create electron-ion pairs while traverse the drift tube. Electrons under  
103 affecting the electric field drift to the wire anode (see figure 4). During the travel they increase  
104 their energy and invoke an avalanche. Therefore they produce a measurable signal.

105 Initial electrons drift to the wire due to the electrical field between the wire and the tube  
106 wall. Electrons ionize gas molecules due to the high electric field around the wire, especially  
107 near the wire when the electric becomes very strong. Subsequently readout electronics process  
108 the signal induced on the wire.

109 The event registers if signal reach some a threshold voltage (Fig. 5). So the value of threshold  
110 is a key factor on the way of searching optimal setting for signal processing procedure.

Табл. 2: STRAW tube parameters

Parameter name	Value
wire	$30\mu m$ gold-plated Tungsten
straw length	$5m$
Voltage	$1750V$
inner tube radius	$9.8 mm$
wire medium density	$19.3 g/cm^3$
Wire tension	$\sim 90 g$
Working tube gas mixture	$Ar70\% CO_230\%$

111 We have to set threshold as low as possible but enough above from noise level to achieve  
112 best rate of true/false detected tracks and highest track registration precision and efficiency.

113 A variation of the signal height introduces a variation in the time when the signal passes  
114 the threshold and is considered to be the main contribution to the STRAW tracker resolution.

115 In the track reconstruction software(GARFIELD [1]) an effective TR-relation is used. It only  
116 describes the relation between the drift time and the distance from the track to the wire, which  
117 differs from the distance to the ionization cluster. The shape of the TR-relation is defined by

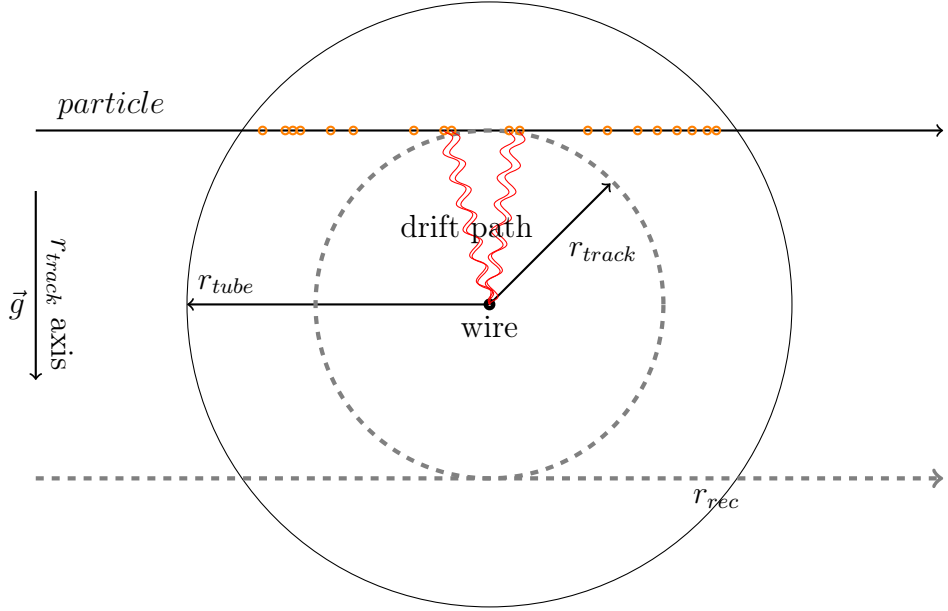


Рис. 4: Schematic view of a particle passing the straw and producing ionization clusters (orange points). The ionization cluster electrons drift to the wire and induce the signal. The closest distance from the track to the wire,  $r_{track}$ , and radius of the straw,  $r_{tube} = 2.45\text{mm}$ , are also indicated.

the drift velocity of the ionization cluster inside the straw. The electric field increases towards the wire, leading to a non linear TR-relation.

The drift time versus the unbiased distance distribution and the result of the fit are shown in Fig. 17a. Noise hits under the main distribution, i.e. at earlier times, are due to primary or secondary particles ( $\delta$ -rays) passing the straw at a closer distance to the wire, consequently producing an earlier signal. Initial clusters along the track are marked by orange points on the figure.

Muon  $\mu$  was chosen as test particle for simulation with energy  $1\text{GeV}$ . You can see some of typical tracks from the  $\mu$  through the tube Fig.10a,10b.

### 3.1 Leakage noise

Every time we deal with different kind of noise. Basically it is noise from leakage current through readout electronics.

As will be discussed further we analyse not the current invoked by particle but the output voltage from amplifier. In GARFIELD we able convolute input current  $I(t)$  with electronic response function (1)<sup>2</sup>

$$f_{resp} = A \cdot (e^{-t/0.005} - e^{-t/0.030}) \quad (1)$$

Noise is very important for every calculations and it makes bit impact on straw precision and straw efficiency. So we can't rely on results until we receive signal and noise from real

---

<sup>2</sup>in this equation  $t$  in nanoseconds

<sup>135</sup> STRAW tube prototypes.

<sup>136</sup> Convolution of input current make it smooth. Usually in typical conditions<sup>3</sup> noise have gauss  
<sup>137</sup> distribution with RMS equal to a amplitude of signal from 2000 electron in the tube - electric  
<sup>138</sup> noise charge (ENC)<sup>4</sup> In fig.5 you can see deposition from noise marked by blue line.

<sup>139</sup> On the Fig.5 The timestamp *Time* = 0 correspond to the time muon hits a tube. The  
<sup>140</sup> convolution function smooths and spreads input current. It mean that the output voltage in  
<sup>141</sup> GARFIELD does not contain part of signal before hit event timestamp.

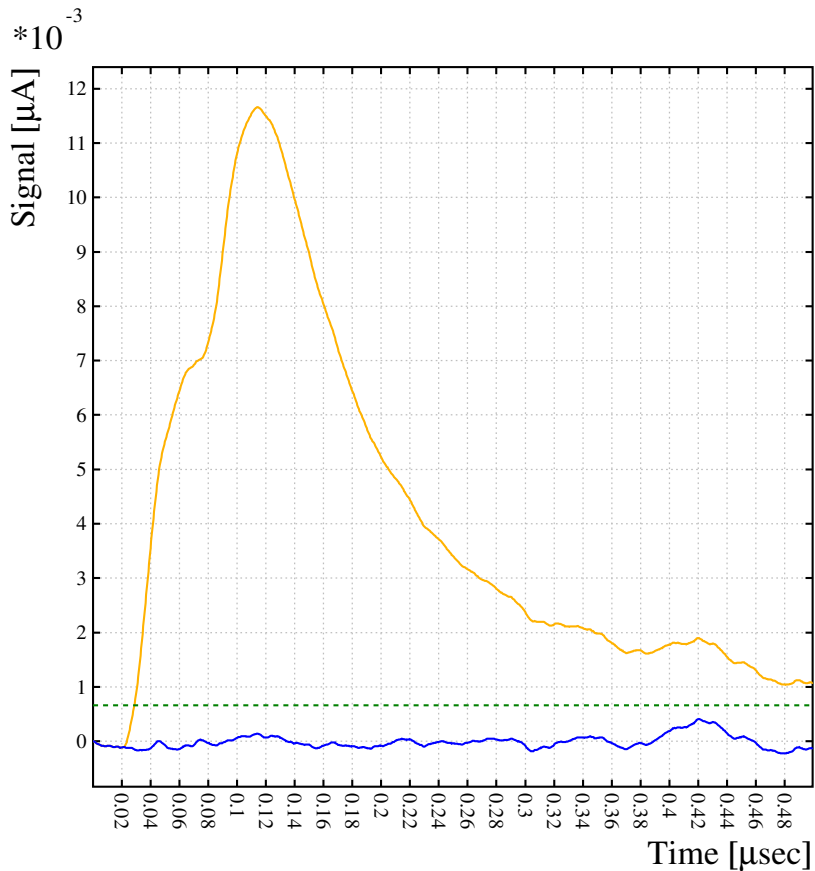


Рис. 5: Example of output signal  $V(t)$  after convolution(front-end electronics) from central track(yellow line). The noise component of the same signal depicted by separate blue line. Grin dashed line is a threshold for trigering drift time and equal to  $5\sigma$  of noise distribution.

## <sup>142</sup> 3.2 STRAW efficiency

<sup>143</sup> The interaction of charge particle with gas molecules have probabilistic nature. For short di-  
<sup>144</sup> stance tracks(somewhere near the tube wall) the probability of tracks that do produce zero  
<sup>145</sup> electron/ion pair becomes significantly high.

---

<sup>3</sup>as in table 2

<sup>4</sup>With testing of real 5 m long straws and ultimate examples of electronics we will measure real noise. But for now is only close to reality suggestion concerning whis.

146      The number of produced ionization clusters directly affects the hit efficiency profile. [2]  
 147      Smaller ionization length increase hit efficiency because of more ionization clusters per length  
 148      unit are producing. In GARFIELD we can easily calculate amount of clusters per track. In fig.  
 149      7b you can see a distribution of number of clusters per central track for our STRAW tube. It  
 150      mean that straw efficiency will be lower near the tube wall(see Fig.6).

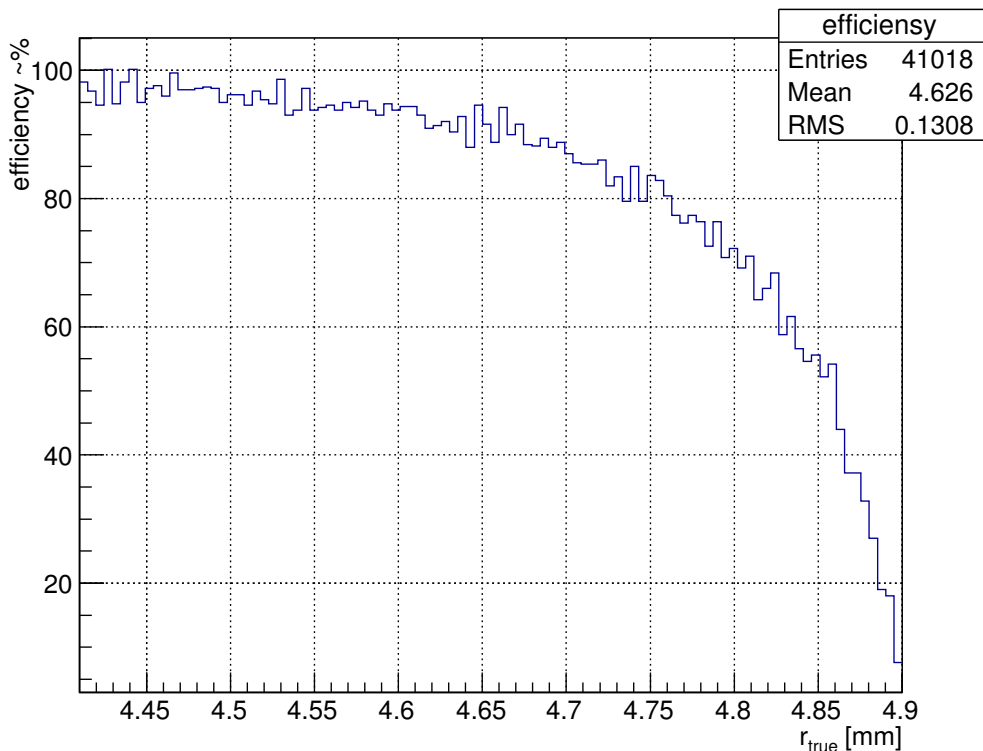


Рис. 6: Straw tube efficiency. Result of homogeneous penetrating periphery of tube by 50k events(scaled down by factor of 5.  $\frac{50k \text{ events}}{100\text{bin}} = 500 \frac{\text{events}}{\text{bin}}$ ).

151      From the Fig.6 we can conclude that the efficiency of tube is 100% almost in whole region  
 152      covered by tube except pre wall region which is quite small. Increasing the gas mixture density  
 153      or increasing the tube radius for the same gas density can increase tube efficiency.

## 154      4    Gain

155      Lets look on avalanche process in the tube. If multiplication occurs, the increasing of the number  
 156      of electrons per path  $ds$  is given by

$$dN = N \alpha ds \quad (2)$$

157      The coefficient  $\alpha$  is determined by the excitation and ionization cross sections of the electrons  
 158      that have acquired sufficient energy in the field. It also depends on the various transfer mechani-  
 159      sm and electric field  $E$  and increases with the field because the ionization cross-section goes up

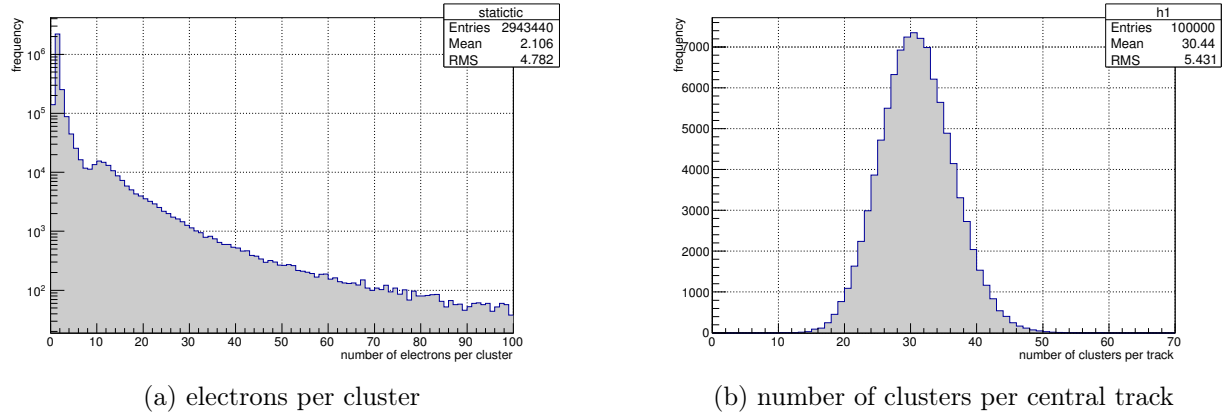


Рис. 7: Statistics info from GARFIELD about track from  $1GeV \mu$ . Tube described in table 2

from threshold as the collision energy  $\varepsilon$  increases. As we can suppose the coefficient  $\alpha$  is of big amount of parameters.

The amplification factor  $G$  on a wire(that is more interesting for us) is given by integrating (2) between the point  $s_{min}$  where the field is just sufficient to start the avalanche and the wire radius  $a$ :

$$G = N/N_0 = \exp \int_{s_{min}}^a \alpha(s) ds \quad (3)$$

GARFIELD can provide us by amplification factor  $G$  for any point of the tube(because  $G$  is coordinate dependent magnitude). The amplification factor is equal almost in whole tube space except neighbourhood near the wire because electric field becomes significantly high only near the wire (see figs 8a, 8b). When the wire is shifted from the center of the cube the electric field in area close to the wire is the same as in centered state. So the amplification factor  $G$  is quite similar in both cases.

Implementation of gain value calculation is not so reliable in GARFIELD(especially fortran version). Gain should be recalculated using Garfield++ (which is newer and take into consideration more effects).

On the Fig. 9 you can see that the gain  $G(V)$  have precisely exponential dependence. This is frankly does not inspire confidence. The difference can be up to 100% (as Rob Veenhof - creator of GARFIELD [1] said).

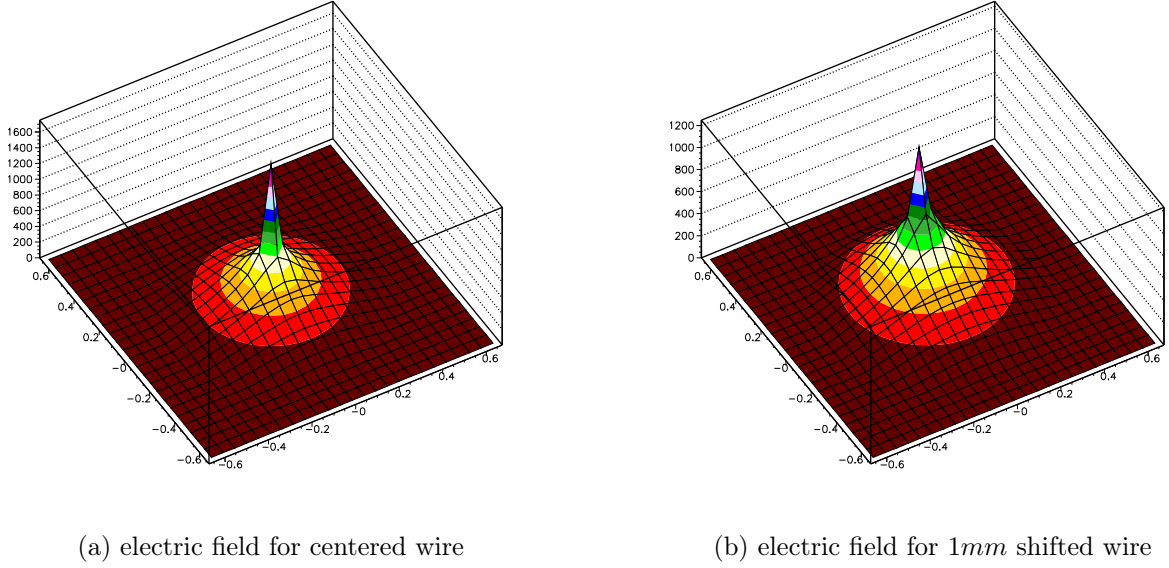


Рис. 8: Electric field intensity map for different wire position in the cube calculated in GARFIELD software. Conditions for those plots are described in table 2

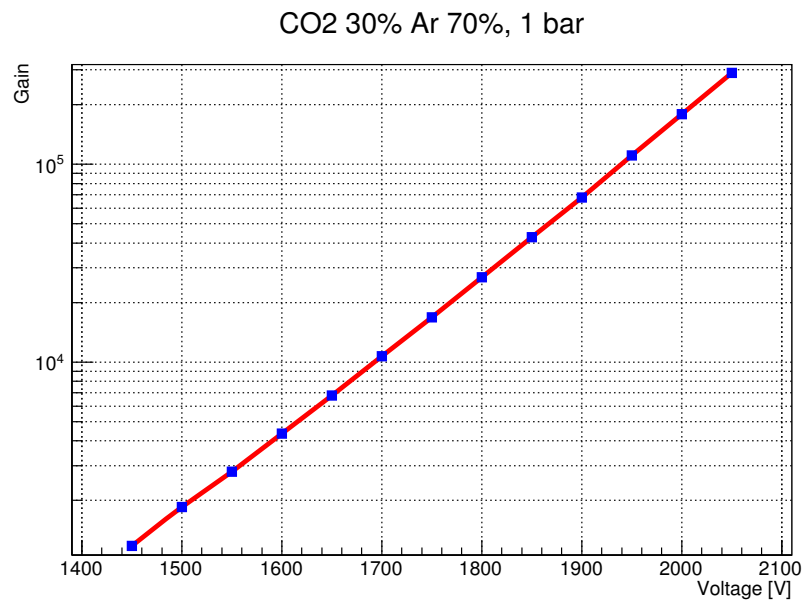


Рис. 9: Dependence of the gain of the voltage applied to the wire. The rest of STRAW tube settings correspond to table 2.

## 177 5 Wire sagging

178 Easy to predict that the displacement of the wire invokes distorting an electric field(see fi-  
 179 ggs 8a,8b) and drift path for electrons/ions inside the tube(see fig.10a and fig.10b). The rt-  
 180 relation for track reconstruction directly depend on the wire position in the tube. So rt-relation  
 181 lose it's previous symmetry(see next sections).

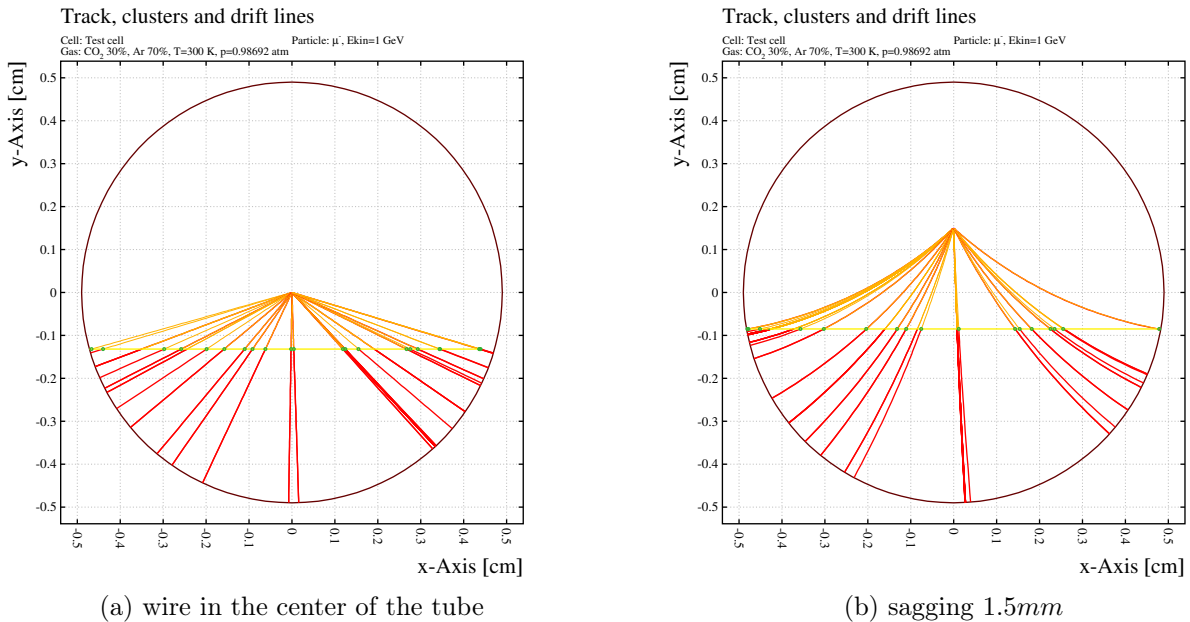


Рис. 10: An example of tracks from the on the tube for different position of the wire from GARFIELD simulations. Initial clusters marker by green. Drift lines for electrons marked by yellow, ions – red lines.

182 The direction of sagging is unpredictable when the wire is centered and the straw has vertical  
 183 orientation. Impact of gravitation field into the wire does not make any effect in this state. But  
 184 we can avoid this ambiguity by setting straws horizontally. This condition is necessary to make  
 185 track reconstruction possible. Even when strung with a pulling force  $T$  close to the breaking  
 186 limit, wires in several metre long tubes will experience a gravitational sag that is large in  
 187 comparison with the achievable accuracy of drift tubes.

188 We estimate significant wire sagging(by comparison to the tube radius) because of wire  
 189 attracts to the tube under affecting of gravitation and electric field force.

190 You can see a profile of wire sagging of 5m length wire in 1cm diameter straw tube and  
 191 1750V voltage on the fig.11 calculated in GARFIELD software [1].

192 The calibration of STRAW tube with sagged wire is more difficult by comparison to the  
 193 mode without sagging.

194 Variation of wire tension, wire radius should be taken into account as high affect factor for  
 195 sag value.

sag profile for 5m long straw

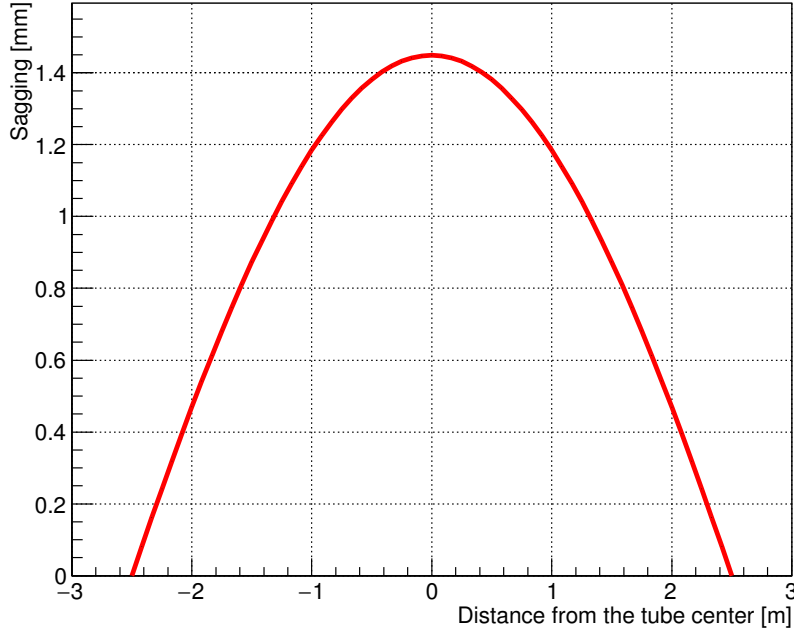


Рис. 11: Wire sag profile under electric and gravitation field calculated in GARFIELD. All options for this straw system are described in table 2.

## 196 6 Sag estimation

197 In this section we have to find out method for assessing sagging. This is key step that makes  
198 track reconstruction procedure possible.

199 At first we have to think on data we can use for such kind of calculations. Much attractable  
200 information we can extract from drift time distribution.

201 The wire sags under electric and gravitation force. Therefore the sag value is differ along the  
202 tube(fig 11). But we can separate collected data for different position along the tube. STRAW  
203 tube detector consist of several parallel layers of tubes at some angle to each other. So we can  
204 easily fix longitudinal position(along the tube) for tracks that cross several crossed tubes(at  
205 least two). Collimation is also possible via scintillator triggering before and after STRAW tube.

206 Lets say we can install our STRAW tube into homogeneous particle flow and save drift time  
207 distribution for some narrow section of the tube. These distributions are different from each  
208 other(see example on Fig.12). The difference between diagrams increasing with sag difference.  
209 So it is good tools for sag calibration.

210 Then we have to bind each drift time distribution with appropriate sag value. This is part  
211 of laboratory work when sag profile measurements can be performed via optical method prior  
212 to the exposition.

213 Distributions on graph 12 contain GARFIELD simulations for some certain wire(not for  
214 section of sagged wire)because of GARFIELD can handle only two-dimensional tasks.

215 Lets say we have an equipment for scanning the tube to measure wire sagging profile. After  
216 profile measurements we divide our tube into sections. Wire position within separate section

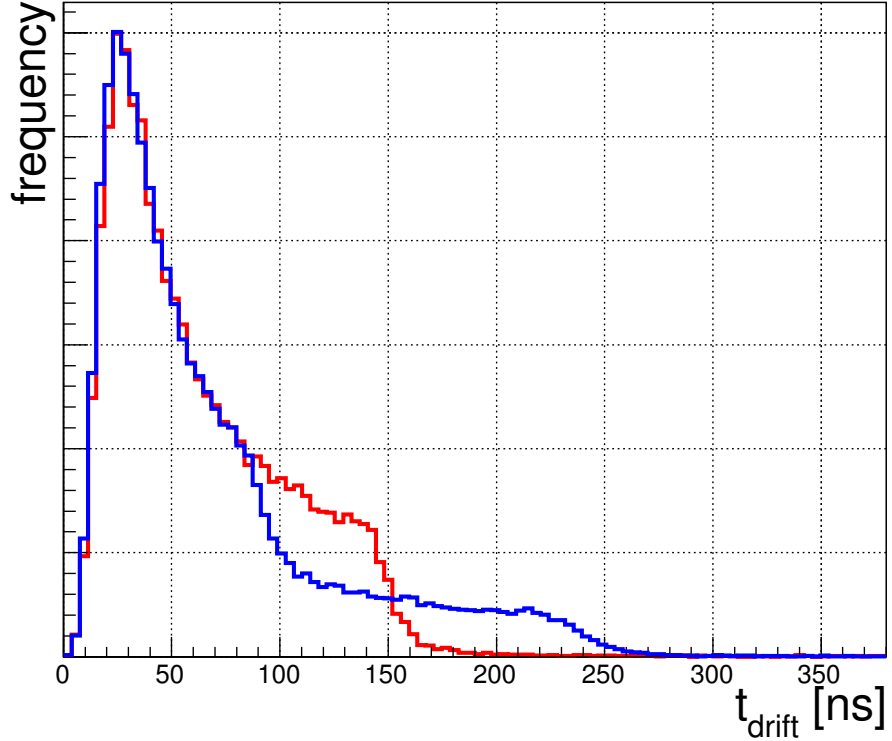


Рис. 12: Drift time distribution for a homogeneous irradiation with a centered wire (red) and for a wire offset of 0.9 mm (blue).

<sup>217</sup> should be within desired precision.

<sup>218</sup> So we need divide our tube into 57 sections (see figure 13) if maximum of wire offset(at the  
<sup>219</sup> center of the tube) is equal to 1.45mm and desired precision is 50 $\mu$ m.

$$N_{halftube} = \frac{1.45\text{mm}}{50\mu\text{m}} = 29; \quad (4)$$

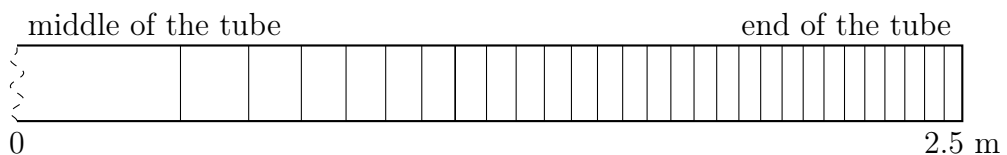


Рис. 13: Tube sectioning. Sag value at the tube center is 1.45mm. Difference of wire sag value from section to section is 50 $\mu$ m

<sup>220</sup> Then we need an exposition of sufficient number of events for every of sections(at least 50k  
<sup>221</sup> events). There can be troubles time of exposition time because square of sections at the end  
<sup>222</sup> of the tube is quite small. So the time of exposition of distant sections will be inversely much  
<sup>223</sup> longer.

224     The next step is to find dependence of dt-distribution shape with wire offset. The point that  
 225    we can evaluate matching between histograms via  $\chi^2$  criteria. As we can see in the figure 14a  
 226    the comparison of  $\chi^2$  has smooth dependence across increasing of wire offset for high statistic  
 227    histograms.

228     First steps for sag estimation are:

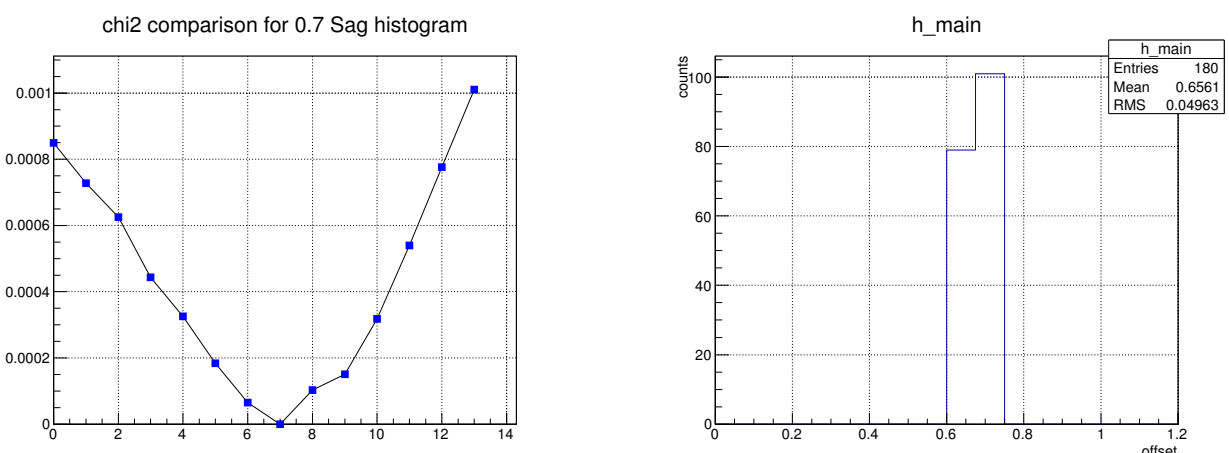
- 229        1. measure wire sag profile via optical method;
- 230        2. make a sectioning for wire sag profile;
- 231        3. collect enough amount of events for every of dt-distribution and save this *core* distribution  
             for further comparisons.
- 233        4. measure dt-distribution for new drift tube section that is subject of study.
- 234        5. calculate  $\chi^2$  criteria for this current dt-distribution with each of core distribution.

235    **6.1 Finding most probable value of wire displacement for certain poi-**  
 236    **nt of the tube**

237    **6.2 Raw method**

238     The simplest method to find  $S$  is to equate it to the corresponding value of best matched core  
 239    DT-histogram.

240     On the figure 14b you can see distribution of such kind of reconstruction. Even for 5k events  
 241    td-distribution in this case the precision can be quite high( $\sim 50\mu m$ ). This method limited by  
 242    core DT-diagram stepping.



(a) Series of  $\chi^2$  of comparison 0.7mm sag core td-distribution with each each of core histograms. 14 core histograms for sag diapason 0...1.3mm with step of  $100\mu m$

(b) Distribution of wire offset reconstruction from 180 series 5k events each. 50k events for *core* template histograms. True bias is 0.63mm. 1 bin = 0.1 mm.

Рис. 14: Wire position(displacement) reconstruction

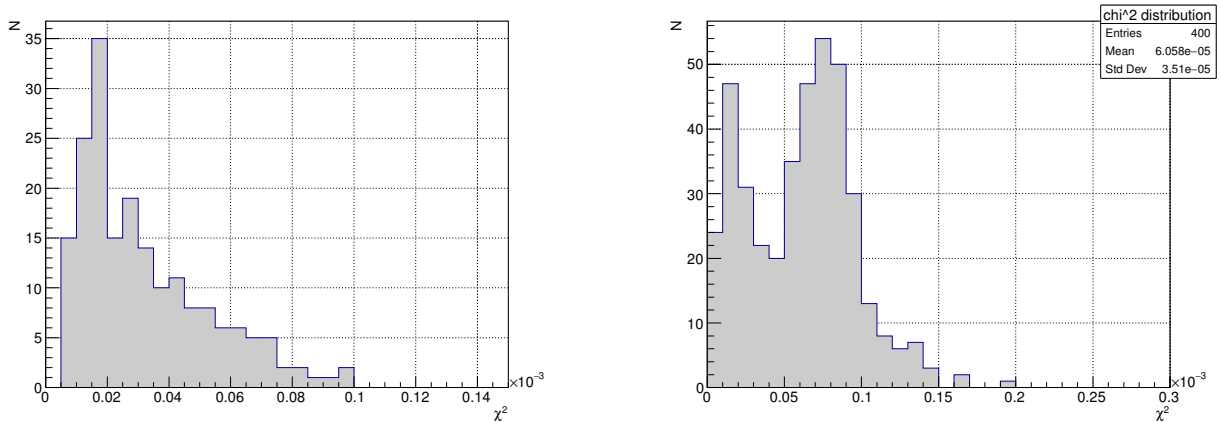
243 **6.3 "Minimum of  $\chi^2$  as linear approximation"**

244 But what is most probable value of wire displacement  $S$  in this case? Probably somewhere  
245 between them. So can we go in more clever way to reach better result? Probably yes.

246 If dependence of  $\chi^2$  criteria of wire displacement  $S$  for near to the true position region  
247 is linear(that certainly is not a true, but as first approximation) than we can easily find this  
248 intermediate value of wire displacement.

249 There we proceed in two steps. The first is raw estimation of wire displacement as in above  
250 mentioned method.

251 For the second step we need to know some additional estimations. The first question is  
252 how small can be  $\chi^2$  it our case? Lets fix statistic on 50k events for one DT-distribution. This  
253 value should a bit depend for different  $S$ . But for now lets consider that it is a constant value.  
254 From the figure 15a you can see distribution of  $\chi^2$  from comparison of 20 DT-distribution<sup>5</sup> for  
255  $S = 0.7\text{mm}$ . Mean value + RMS of distribution is  $5.3 * 10^{-5}$ . So if some of the  $\chi^2$  is higher  
256 than this threshold than we go for second stage.



(a)  $\chi^2$  distribution of comparison of 20 DT-distributions diagrams each other( $C_{20}^2 = 190$  combinations)

(b)  $\chi^2$  distribution of comparison DT-distribution histograms  $0.6\text{mm}$   $S$  vs  $0.7\text{mm}$

Рис. 15: Comparison of  $\chi^2$  distributions for self-comparison of DT-distribution diagram.

257 On the figure 14b you can see distribution wire sag calculation for 180 histograms with 5k  
258 events statistic. Precision in this case  $\sim 50\mu$ . The algorithm of sag estimation is pretty simple:  
259 wire offset value equal to the best match between *test* and *core* histogram.

260 After we know sag value at some points of the tube or every where we can make one awesome  
261 collective analysis. The smoothing of wire offset value along the tube will give us much more  
262 precision results.

263 From the Fig.15b the distribution of  $\chi^2$  for adjacent point have narrower distribution by  
264 comparison to "self-comparison" $\chi^2$  distribution. Therefore method of reconstructing of wire  
265 offset that based on comparison of DT-distribution histogram can find wire offset much precisely.

<sup>5</sup>pair comparison give us  $C_{20}^2 = \frac{20!}{2!18!} = 190$  different combinations

## 266 6.4 Practical measurements of DT-distribution

267 We need second detector that can measure position of muon that hit STRAW tube. It can be  
 268 Si strip sensor based detector or detector based on scintillation with the same destination.

269 Each kind of detector have it's own advantages and disadvantages. The potential cell unit  
 270 (strip or pixel) of Si detector will be smaller than in scintillator but also is much expensive. At  
 271 the current stage we deal with 1cm diameter tubes. So scintillator is primal target. But it can  
 272 shift to the Si sensors if scintillators will not provide satisfied precision.

273 Preliminary chem of DT-measurements you can see on the picture Fig.16

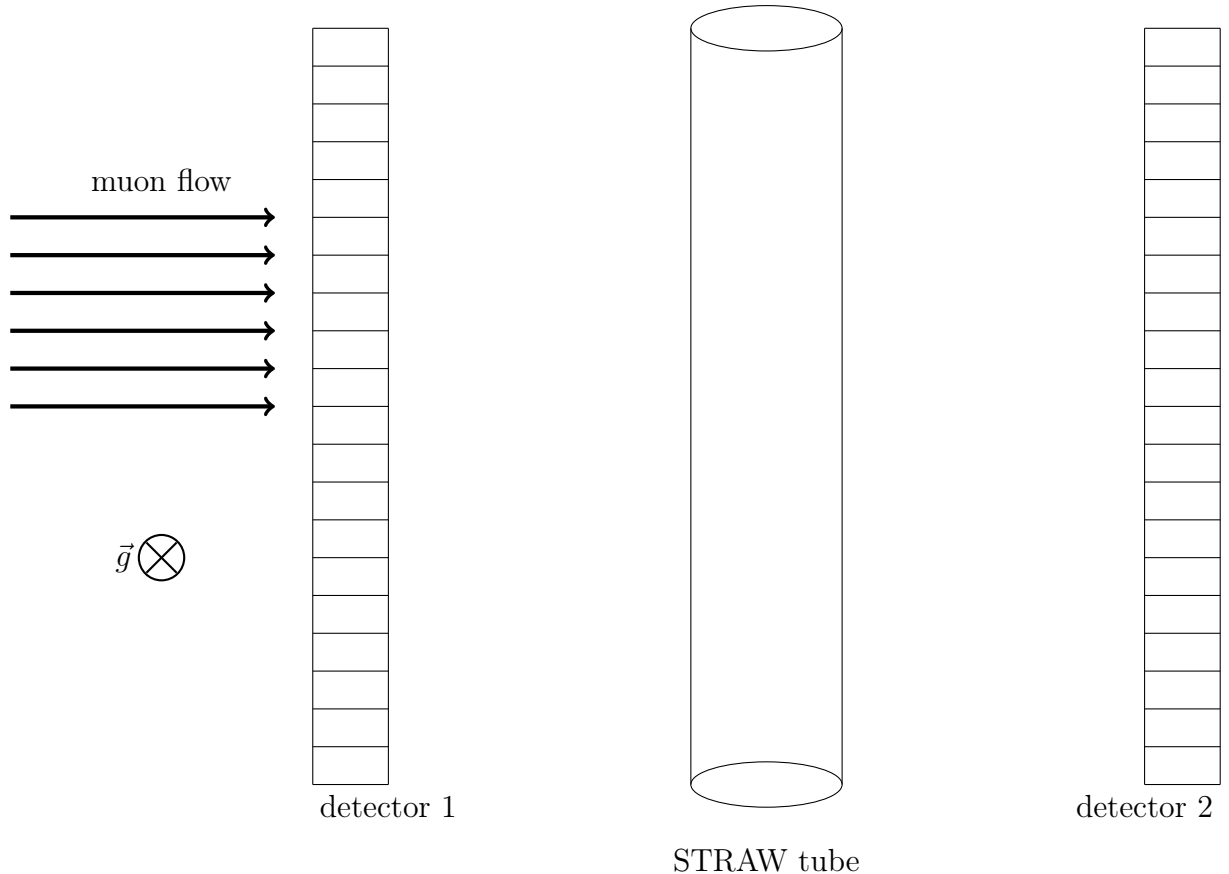


Рис. 16: principal layout of measurement of core DT-distribution histogram

274 In this method detector before tube (D1) and detector placed after the tube(D2) in total  
 275 should provide sufficient precision for track reconstruction to be able distinguish tracks for  
 276 different section of the tube (approximately as shown on the Fig. 13). Muon flow should be  
 277 homogeneous and so D1 and D2 also should cover full acceptance of the tube.

278 The profile of wire sagging can be measured by optical method. Wall of is very thin, so it  
 279 can be simplest way to get sag profile.

## 280 7 Track reconstruction

281 The time between the track hit time stamp and the signal rising edge is a measure of *drift time*  
 282 of these electrons. The relation between the *drift time* and the distance from the track to the  
 283 center of the tube(wire while no sag for centered wire) is called *drift time - distance* relation or  
 284 *tr-relation*.

285 The drift time  $t$  is a function of track position (relative to the wire) and electric field along  
 286 the drift trajectory.

287 Assumed that the working position for straws will be parallel to the particle bunch, and  
 288 acceptance of particle spreading will not be significantly big. So tracks will be collinear each  
 289 other within every separate STRAW tube unit.

290 Summing the above mentioned we have one dimension task – reconstruct tracks on vertical  
 291 axis<sup>6</sup> (see examples of outcome tr-distribution  $t = t(r, s = 0)$  in Fig.17a and Fig.17b) even the  
 292 wire sagging. Sagging will be always down thanks to gravitation force  $\vec{g}$ .

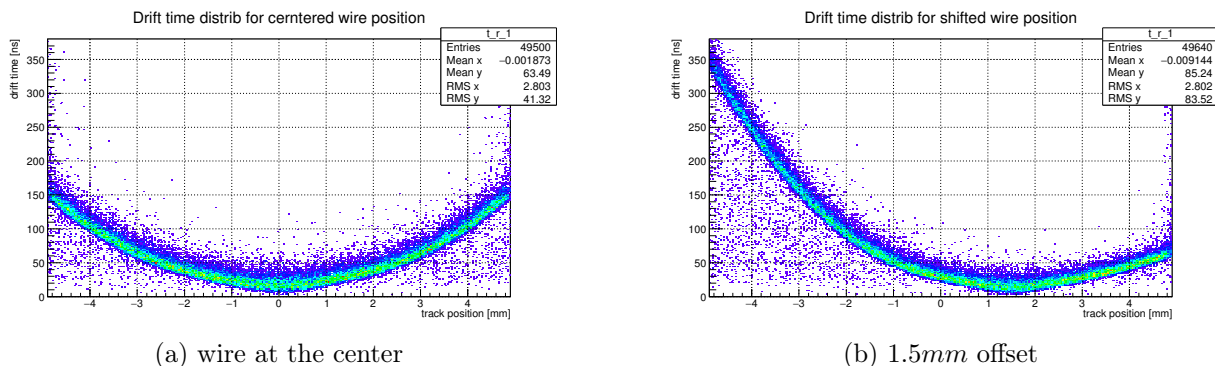


Рис. 17: Distribution of drift time  $t_{drift}$  as function of track position  $r_{track}$  relatively to the tube center

293 The rt-relation is differ along the tube because different wire position  $s$ . Thus we have for  
 294 the drift time

$$t_{drift} = t_{drift}(r_{track}, s) \quad (5)$$

295 The idea to STRAW tube is to find the inverse dependence

$$r_{track} = r_{track}(t_{drift}, s) \quad (6)$$

296 From the section "Sag estimation"we can find sag profile for straw. Therefore the rt-  
 297 calibration becomes 1 dimension less:

$$r = r(t, s = const) \quad (7)$$

### 298 7.1 How drift time resolution depend on wire offset?

299 Distorting of electric field inside the tube invoked by wire displacement from the center position  
 300 will make an effect on drift time. Here we are going to estimate magnitude of drift time change.

---

<sup>6</sup>An example of single track reconstruction which explains the approximate procedure of reconstruction you can see on Fig.4

301 As was noted above we make a binning for our data along the  $r_{track}$ (fig. 17a, 17b). The  
 302 resolution at every bin is RMS of every bit digram (fig.??).

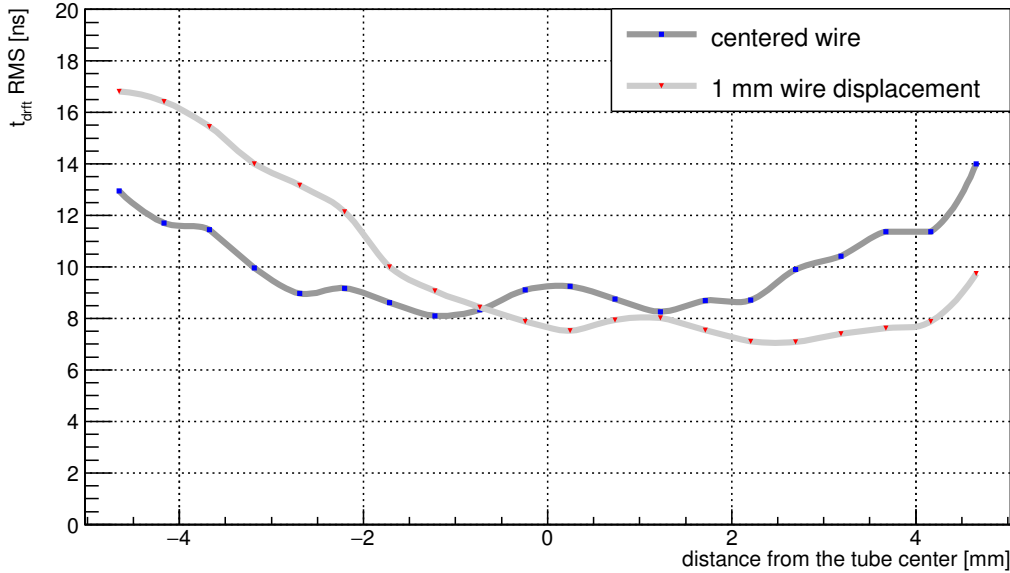


Рис. 18: Resolution of drift time as a function of distance from the wire.

303 We are dealing with probabilistic nature of clustering that spread rt-relation from thin line.  
 304 The leakage noise is also present in calculation but the effect of it is not very high(especially in  
 305 this calculation).

306 Every plot of output current (see fig. 5) consist of 1000 equidistant frames. The threshold is  
 307 set to  $5\sigma$  of noise. Leakage noise make effect on drift time measurements in case its amplitude  
 308 becomes higher than threshold value in range from  $t = 0$  to  $t = t_{drift}$ . At five-sigma there is  
 309 only one chance in nearly two million that a random fluctuation would yield the result. The  
 310 drift time for tracks close to the tube edge can be up to 150ns and 300ns in case wire displaced.  
 311 The probability to meet noise above threshold value is less than 0.02%.

312 Another source of noise points on tr-distribution comes from  $\delta$ -electrons that cause  
 313 secondary ionisation in tube volume. The impact do only those electrons which are emitted  
 314 in the direction of the wire(see example on fig.19a).

315 The number of events out of TR-ralation because of  $\delta$ -electrons is quite small. Especially  
 316 percentage of events where  $\delta$ -electrons make effect on drift time is less than 1% of total number  
 317 of events in GARFIELD simulations.

318 Tube wall is very thin but particle still can cause  $\delta$ -electrons when crossing it. GEANT4  
 319 studies show that such kind effect also presents in interaction of muon with tube volume, and  
 320 percentage of events with  $\delta$ -electron that affect drift time even less than 0.2%.

## 321 7.2 Finding of rt-relation

322 The rt-relation depict relation between drift time and track position. The idea is to find the  
 323 best fit of give data to achieve higher resolution and avoid systematic errors.

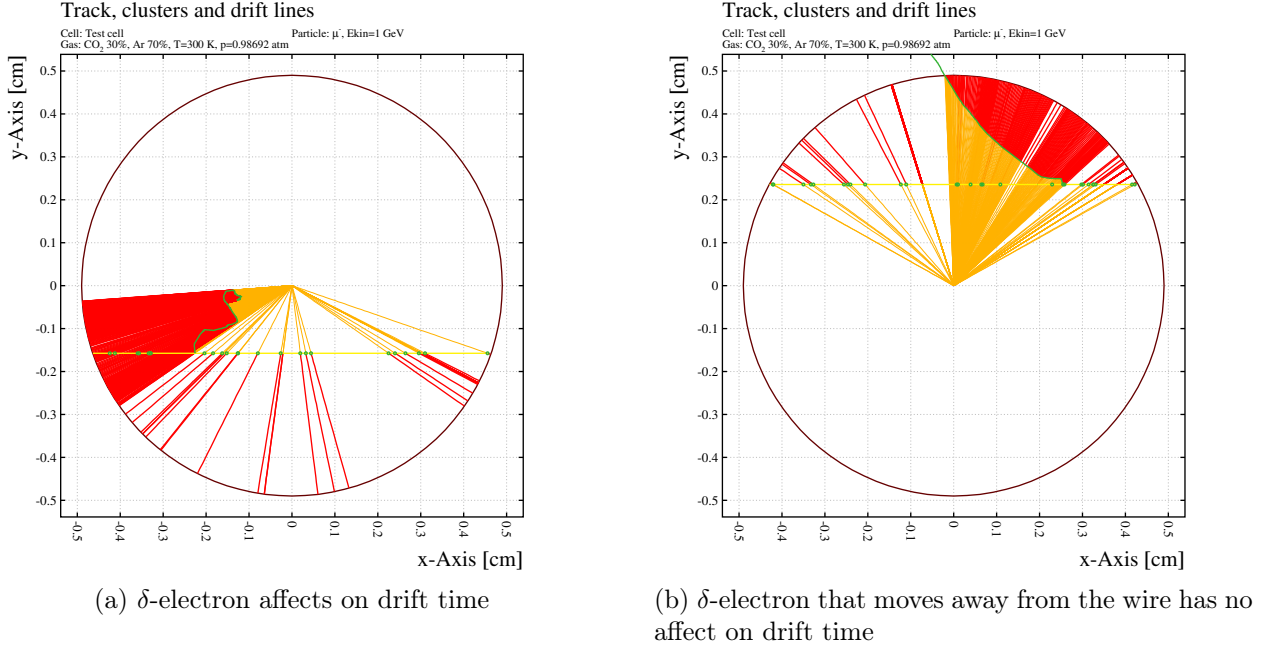


Рис. 19: Garfield simulation with  $\delta$ -electron presence. Red lines - ion trajectory, yellow - electrons. Trajectory of  $\delta$ -electron marked by green curve line.

The problem that we have to minimize influence of noise while fit. One suppose that the noise have approximately homogeneous distribution of points that locates below the main line of distribution. Consequently we can filter it by fitting only points from regions with local point density higher than some threshold value. Another way is to make a binning our distribution along the track position and fit every 1-D histogram by Gaussian. The fit points of Gaussian mean values by fit function.

Nevertheless our data contain very small amount of "non-track"points.

TR-relation is asymmetry relatively to the  $r = 0$  almost in all cases except wire in the center of the tube. Therefore we have to calibrate for every of branches. It means we need to find two track positions for every of drift time value and reject one of them in further data processing stages.

In previous section we found way to measure wire sag profile. So we can use this trick in present stage for separating data into "right" and "left" branch. Every of branches we will calibrate separately.

Lets suppose we can fit every of tr-diagram by pair of analytic fit function (8):

$$t(r_{track}) = e^{a_0 + a_1 r_{track}} \quad (8)$$

If the figure ?? you can see tr-relation. Fitting is not perfect because of using simple fit function template (8). But we will use reverse to the (8) relation, because we have to find  $r_{track}$  from known  $t_{drift}$ . We can do it be because the aim of this studies is not a precision calibration but global evaluation affect of wire sagging into total result.

As you can see in the figure ?? red fit line does not cover whole drift time spectre. So events with drift time less than covered range(less than  $\sim 20\text{ns}$ ) counts as track through the wire:

$$r_{track}(t_{drift} < t_{min}) = r_{wire \ pos} \quad (9)$$

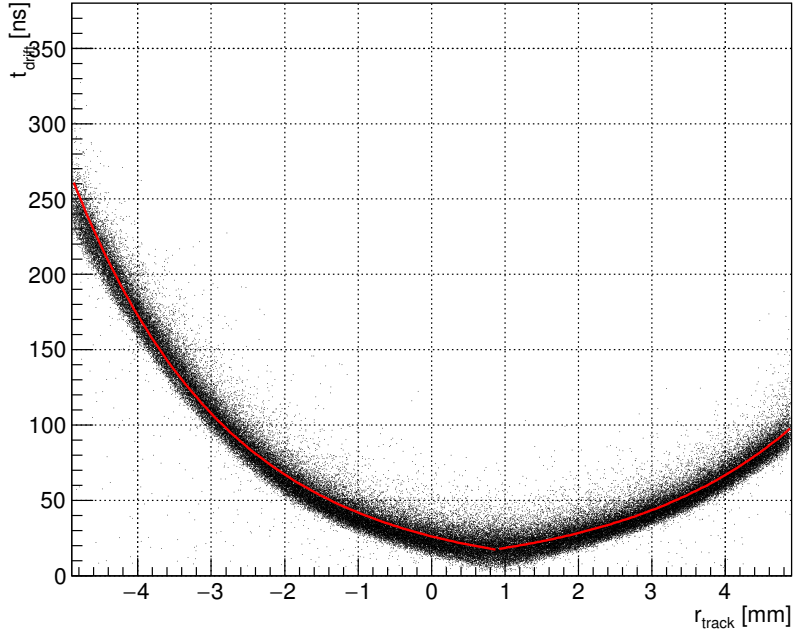


Рис. 20: TR-relation fitting for 0.9mm wire offset value

345 where  $t_{min} = \min(t_{drift}(r_{track}))$ ,  $r_{track} = \overline{(-r_{tube}, r_{tube})}$ . Respectively tracks with drift time  
 346 higher than maximum of fit function range artificially counts as tracks with near tangents to  
 347 the tube position  $r_{track} = \pm r_{tube}$  (because efficiency decreases near the tube wall down to 20%).

### 348 7.3 Track reconstruction precision

349 Obviously precision is head factor when during we decide design of detector.

350 The STRAW tube tracker should be as light as possible to avoid multiple scattering on  
 351 structural components of detector. But design should be changed within reason if precision  
 352 suffers from this<sup>7</sup>.

353 How precision of track reconstruction depends on wire position(wire displacement)?

354 As you can see on figure ?? there are no significant difference of track reconstruction preci-  
 355 sion between two mode of wire location despite of the increasing drift time for displaced wire  
 356 position(with almost factor of two). The highest resolution( $\sim 0.1mm$ ) near the tube wall and  
 357 worst value  $\sim 0.6mm$  is near the wire because the clustering effect. Higher gas pressure should  
 358 resolve this problem.

---

<sup>7</sup>Especially design with no sagging works well for experiment NA62 []. But they have more than 2 times shorter straw when tube have insert in the middle of the tube. So sagging becomes negligible in this case.

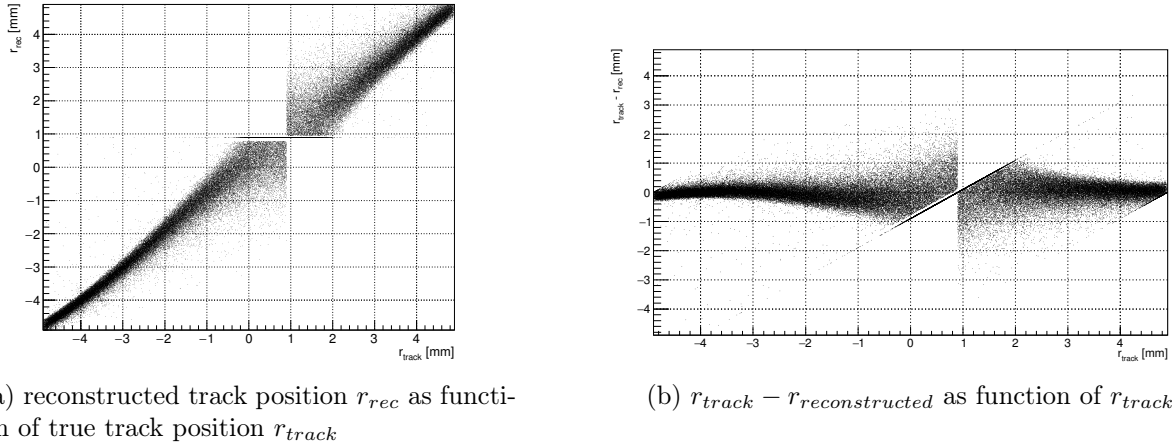


Рис. 21: Distributions of matching of track position to their reconstructed value.

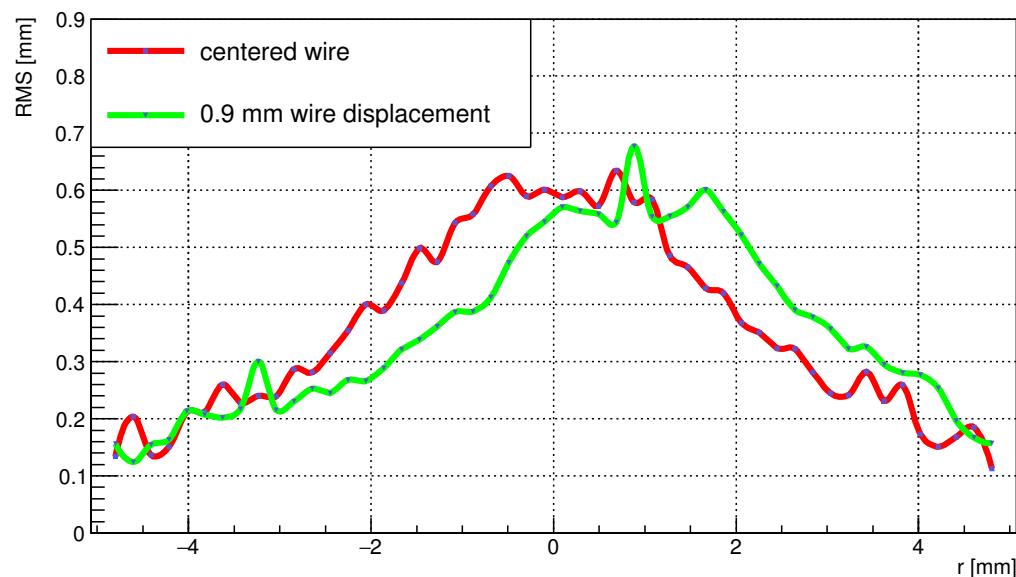


Рис. 22: Comparison of track reconstruction precision for two wire position. Value of precision at every point means RMS of data sample near corresponding track position  $r$ . Red line corresponds to the centered wire position, green line – to the 0.9mm sagged wire position.

## 359 8 Measurements

360 We made measurements of some important drift tube parameters. We had tube of  $\sim 50\text{cm}$   
 361 length. But despite of short tube length we made there the length of the tube is not important.

362 The tube was manufactured in Dubna(Russian Federation) and was placed into the appropriate  
 363 mechanics which include tube fixing, channels for supply of gas mixture, connector for  
 364 grounding to the tube walls and connector for High Voltage (HV) supply.

365 The whole system is not compact, therefore we could not avoid the parasitic capacities. Now  
 366 we will not go into details about it, as we have nothing to compare with because the system is  
 367 non-separable.

368 The scheme of gas supply, circulation and control in the tube is shown in the Fig.23.

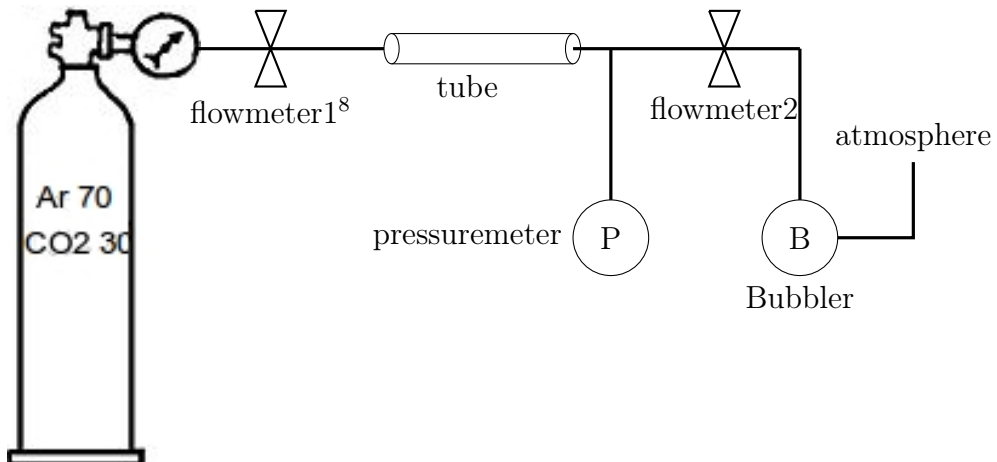


Рис. 23: Gas circulation scheme and circuit of connection of flow control through the drift tube

369 The electric scheme of the drift tube connection is shown in the Fig.24.

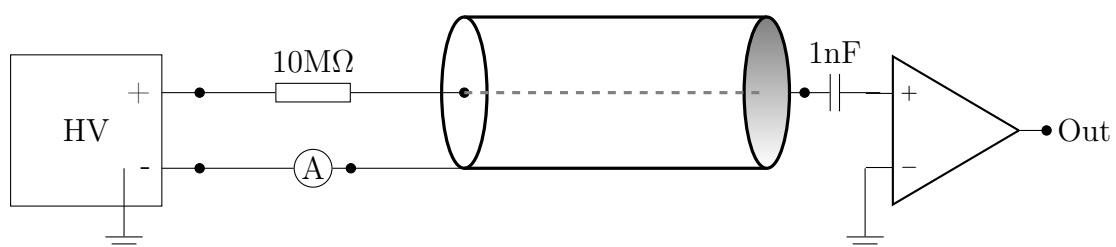


Рис. 24: The electric scheme of the drift tube connection

370 As it is seen above, the scheme is very simple.

371 For our research we used a source  $\text{Fe}^{55}$  witch is suitable for a drift tube calibration. In our  
 372 case  $\text{Fe}^{55}$  serves as a photon source with almost monochromatic spectra with energy 5.9 keV.

373 The most important parameter witch we have to measure a Gain  $G$  (3).

374 The idea is to measure a charge that goes thought the tube electric circuit per unit of time  
 375 and then find a Gain. We assume that a current  $I_0$  though the ampere meter(see fig. 24) is  
 376 constant when the radioactive source is absent. The current is non-zero when the tube detects  
 377 background particles(for example atmospheric muon flux) or when a leakage current is present.

378 Therefore, with the presence of a source  $Fe^{55}$  all surplus of the current  $\Delta I = I - I_0$  in the drift  
 379 tube circuit occurs because of gamma ray detection.

380 On the other hand, we can write  $\Delta I$  in terms of initial amount of electrons and Gain in  
 381 the following form :

$$\Delta I = GN_0e, \quad (10)$$

382 where  $G$  – Gain;  $N_0$  - number of initial electron-ion pairs per second;  $e$  - charge of electron  
 383 in C.

384 On the other hand we can express  $N_0$  as:

$$N_0 = R \cdot \langle n \rangle = R \cdot \sum_n np(n) \approx R \int_0^{\infty} np(n)dn; \quad (11)$$

385 where  $p(n)$  is a probability that the photon with energy 5.9 keV after interaction with  
 386 argon atom will create  $n$  electron-ion pairs;  $R$  is a rate [Hz], as we need to find the amount of  
 387 electron-ion pairs per one second.

388 The calculation of the distribution  $p(n)$  in GARFIELD is shown in Fig.???. In the figure we  
 389 can see the two peaks: the main photopeak and the smaller escape peak. The escape peak for argon  
 390 is known to be 3.2 keV less than the primary peak. An escape peak is formed by a number  
 391 of photon interactions in the gas resulting in one primary ionization electron and a re-emitted  
 392 X-ray with a long mean free path.

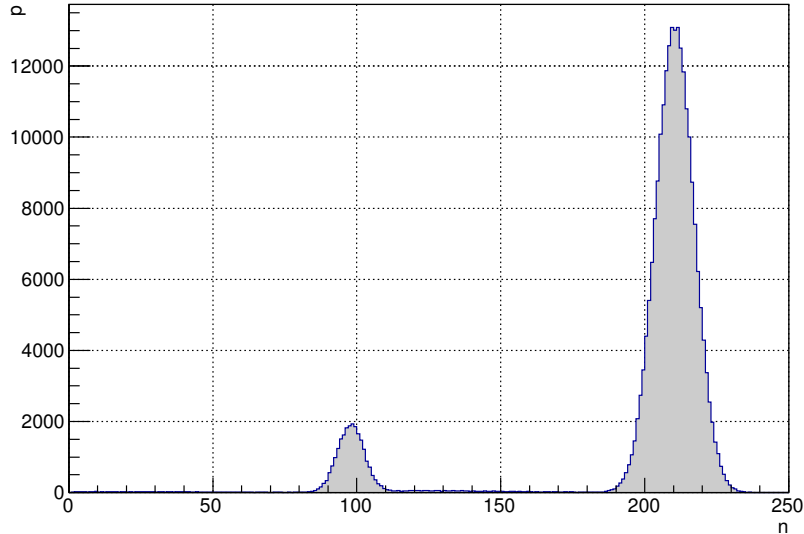


Рис. 25:  $p(n)$  distribution

393 The realisation of a measurement is very simple. On the output of amplifier(see Fig.24)  
 394 the signal goes to the discriminator with trigger threshold on the level enough for a signal  
 395 detection and big enough for noise neglecting. The signal from discriminator goes into counter  
 396 in rectangle form. The counter triggering for the rising edge. This scheme has a small dead

397 time  $0.5\mu s$ , therefore for the signal frequency of  $R \sim 5000 \frac{\text{events}}{\text{second}} \approx 200 \frac{\mu s}{\text{event}}$  the amount of non  
 398 counted signal is negligibly small.

399 For the first gain estimation we assume about avalanche superposition and linear amplitude  
 400 dependence of final signal on the amount of initial electrons(later we will show that this is not  
 401 true).

402 From the distribution in Fig.25 we can find  $\langle n \rangle = 197.87$  for average amount of primary  
 403 electron because of photon(5.9keV) interaction with atoms of a gas  $Ar70\% + CO_230\%$ .

404 The results of measurements are shown in the table 3. The Gain curves G(V) for several  
 405 pressure values are shown in the Fig.26.

Gain(no cor)	P[bar] (U[V])	HV [V]	Thr [mV]	I [nA]	RMS [nA]	Rate [Hz]
11138	1.0(0.857)	1600		1.7700	0.0919	=
18196	1.0(0.857)	1650		2.8915	0.1598	=
29255	1.0(0.857)	1700	32	4.6490	0.2328	4965.9
47012	1.0(0.858)	1750		7.4707	0.4380	=
73159	1.0(0.857)	1800		11.6257	0.5630	=
9885	1.106(0.906)	1650		1.6921	0.1099	=
15747	1.106(0.905)	1700		2.6955	0.13381	=
25275	1.106(0.905)	1750	32	4.3263	0.1975	5349.0
39887	1.106(0.906)	1800		6.8274	0.2841	=
61359	1.106(0.906)	1850		10.5028	0.4567	=
9260	1.205(0.951)	1700		1.6921	0.1053	
14536	1.205(0.951)	1750		2.6562	0.1274	
22991	1.205(0.951)	1800	32	4.2012	0.1900	5710
35777	1.205(0.951)	1850		6.5376	0.2880	
54684	1.205(0.951)	1900		9.9924	0.5284	
5444	1.309 (0.998)	1700		1.03	0.06	
8351	1.309 (0.998)	1750		1.58	0.14	
13267	1.309 (0.998)	1800		2.51	0.12	
20615	1.309 (0.998)	1850	32	3.90	0.15	5987
31716	1.309 (0.998)	1900		6.00	0.29	
48102	1.309 (0.998)	1950		9.10	0.38	
69987	1.309 (0.998)	2000		13.24	0.50	
100751	1.309 (0.998)	2050		19.06	0.78	

Табл. 3: Gain measurements

## 406 8.1 Experimental spectra from the source Fe55

407  $Fe^{55}$  is a source of gamma-rays with energy of 5.9 keV. Each signal at the output of amplifier  
 408 differs by amplitude in dependence of initial electron number. Therefore, according to the

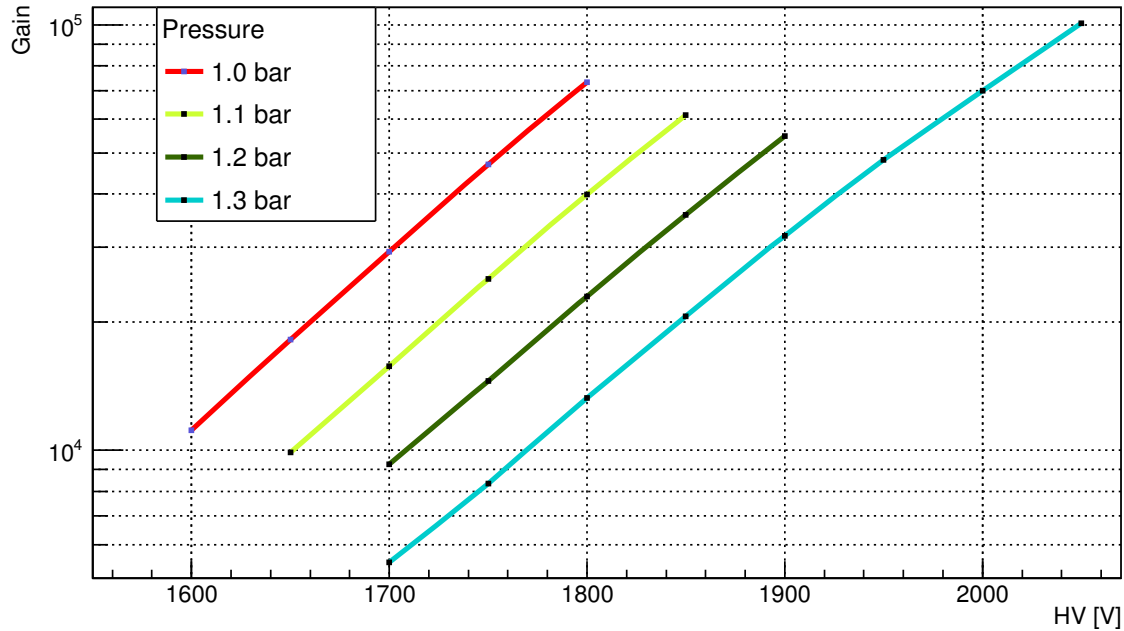


Рис. 26: Gain experimental curves for several values of gas pressure in the drift tube.

409 calculated in GARFIELD spectra  $p(n)$  (see Fig.25), it is expected to see two peaks in exper-  
410 imental spectra.

411 For spectra measurements we first have to get a match between a certain signal and the  
412 amplitude on the output of the drift tube. In our case such a quantity is an integral from a  
413 signal on during the time of a signal.

414 The amplified signal from the output of the amplifier is sent in parallel through the linear  
415 splitter to the discriminator and delay system. With the signal from discriminator the sampling  
416 signal and busy signal is formed. During the busy signal the analysing system does not accept  
417 the signal from the drift tube (this is a dead time for this detector system). The delayed signal  
418 from the amplifier integrates during the sampling signal and then digitalizes with 10-bit ADC.  
419 After digitalizing the signal is sent through the optical channel to PC, where the data is recorded  
420 into separate ROOT-file.

421 The stages *sampling + storing* are time-consuming and a dead time in this case is bigger than  
422 an average time interval between events in the tube (with current detector system) therefore is  
423 a big probability to miss detecting an event.

424 The sampling stage is built in such a way to calibrate for pedestal shelf voltage from the  
425 integrator. On the final histogram it will look as a small peak. We will calibrate exactly with  
426 regard to it. The second control point is a gamma-ray 5.9 keV photo peak from the source  $Fe^{55}$ .

## 427 8.2 Space charge effect

428 Photons from  $Fe^{55}$  of energy 5.9 keV create  $\sim 200$  electron-ion pairs as a result of photoeffect  
429 with  $Ar70\% + CO_230\%$  gas mixture. As we have a strong electric field between anode and

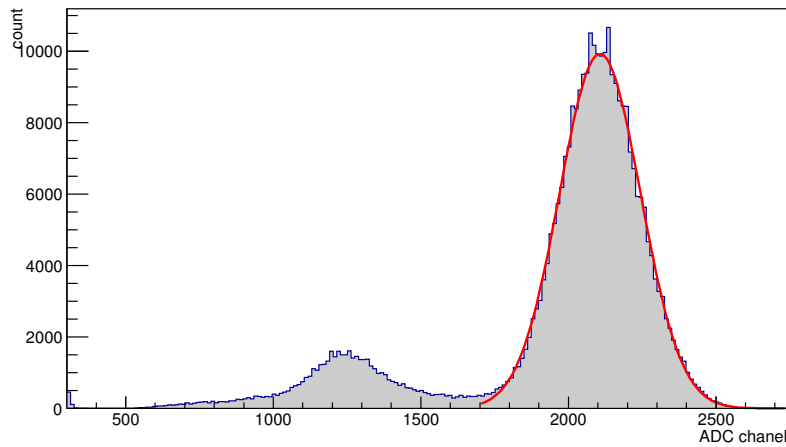


Рис. 27: Experimental spectra from  $Fe^{55}$ .

point of reference	channel	electrons per cluster(simulations)
zero pedestal ( <i>gauss</i> $\mu \pm \Delta\mu$ )	$301.1 \pm 0.3$	0
5.9 keV	$2107.4 \pm 0.3$	$210.42 \pm 0.01$
escape peak	$1253.3 \pm 0.9$	$97.99 \pm 0.03$

Табл. 4: Coordinates of peaks from Fig.27 and Fig.25

430 cathode such electron cloud starts to drift toward a wire. The external field distorts as any  
 431 space charge creates its own e/m field. As a result, partial avalanches per initial electron of a  
 432 cloud creates an avalanche of size smaller than from a single-electron cloud(as in case muon  
 433 ionisation).

434 Such an effect indeed was observed. If we suppose a linear dependence of output signal  
 435 amplitude from number of initial electrons a relative position for experimental peak should be  
 436 located at(calibration relatively to the photopeak):

$$channel_{escapePeak} = \frac{2107.4 - 301.1}{210.42} 98 + 301.1 = 1142.3 \neq 1253.3, \quad (12)$$

<sup>437</sup> **9 Додаток**

<sup>438</sup> **9.1 pressure meter**

<sup>439</sup> For the pressure measurement inside of drift tube we used pressure transmitters from  
<sup>440</sup> SensorTechnics<sup>®</sup>. The devise is marked by ID:CTE9005AQ4, so we used appropriate datasheet  
<sup>441</sup> from the manufacturer [5].

<sup>442</sup> According to datasheet and marking, this pressure transmitter is designed for pressure  
<sup>443</sup> measurements in the interval  $0 \dots 5 \text{ bar}$ . But on the transmitter is marked an interval  
<sup>444</sup>  $0 \dots 3,5 \text{ bar}$ . So to be able to use this devise, we additionally calibrated it.

<sup>445</sup> For this purpose we used two control points: the output current value for atmospheric  
<sup>446</sup> pressure at that point (727 mmHg) and a current for a vacuum. To get a vacuum we used a  
<sup>447</sup> pump which decreases a pressure to the value  $< 0.001 \text{ bar}$  which we consider as a vacuum.

Табл. 5: Control points for calibration of pressure transmitter.

pressure [bar]	voltage[V]
$<0.001$	0.405
1	0.858

<sup>448</sup> Therefore the voltage dependence taken on a resistor  $100\Omega$  depends on a pressure as:

$$V = 4.05 + 0.453 \cdot P[\text{bar}] \quad (13)$$

$$P[\text{bar}] = -0.894 + 2.2075 \cdot V \quad (14)$$

## 449 Література

- 450 [1] <http://garfield.web.cern.ch/garfield>
- 451 [2] thesis Kozlinskiy.pdf
- 452 [3] Technical Proposal from 8 april 2015: arXiv:1504.04956v1
- 453 [4] F. Hahn, F. Ambrosino, A. Ceccucci, H. Danielsson, N. Doble, F. Fantechi, A. Kluge, C.  
454 Lazzeroni, M. Lenti, G. Ruggiero, M. Sozzi, P. Valente, and R. Wanke. NA62: Technical  
455 Design Document. Technical Report NA62-10-07, CERN, Geneva
- 456 [5] DataSheet for Pressure transmitters for corrosive liquids and gases CTE/CTU9000 series.  
457 [http://www.first-sensor.com/cms/upload/datasheets/DS\\_Standard-CTE-CTU9000\\_E\\_11509.pdf](http://www.first-sensor.com/cms/upload/datasheets/DS_Standard-CTE-CTU9000_E_11509.pdf)
- 459 [6] W. Bonivento, A. Boyarsky, H. Dijkstra, U. Egede, M. Ferro-Luzzi, B. Goddard, A.  
460 Golutvin, D. Gorbunov, R. Jacobsson, J. Panman, M. Patel, O. Ruchayskiy, T. Ruf, N.  
461 Serra, M. Shaposhnikov, and D. Treille. Proposal to Search for Heavy Neutral Leptons at  
462 the SPS. Technical Report CERN-SPSC-2013-024. SPSC-EOI-010, CERN, Geneva (Oct,  
463 2013).